

Hybrid moiré excitons and trions in twisted MoTe₂-MoSe₂ heterobilayers

Shen Zhao,¹ Xin Huang,^{2,3,1} Roland Gillen,⁴ Zhijie Li,¹ Song Liu,⁵ Kenji Watanabe,⁶ Takashi Taniguchi,⁷ Janina Maultzsch,⁴ James Hone,⁵ Alexander Högele,^{1,8} and Anvar S. Baimuratov¹

¹*Fakultät für Physik, Munich Quantum Center, and Center for NanoScience (CeNS), Ludwig-Maximilians-Universität München, Geschwister-Scholl-Platz 1, 80539 München, Germany*

²*Beijing National Laboratory for Condensed Matter Physics, Institute of Physics, Chinese Academy of Sciences and School of Physical Sciences, CAS Key Laboratory of Vacuum Physics, University of Chinese Academy of Sciences, Beijing 100190, P. R. China*

³*School of Physical Sciences, CAS Key Laboratory of Vacuum Physics, University of Chinese Academy of Sciences, Beijing 100190, P. R. China*

⁴*Department of Physics, Friedrich-Alexander Universität Erlangen-Nürnberg, Staudtstraße 7, 91058 Erlangen, Germany*

⁵*Department of Mechanical Engineering, Columbia University, New York, New York 10027, United States*

⁶*Research Center for Functional Materials, National Institute for Materials Science, 1-1 Namiki, Tsukuba 305-0044, Japan*

⁷*International Center for Materials Nanoarchitectonics,*

National Institute for Materials Science, 1-1 Namiki, Tsukuba 305-0044, Japan

⁸*Munich Center for Quantum Science and Technology (MCQST), Schellingstraße 4, 80799 München, Germany*

(Dated: April 12, 2024)

We report experimental and theoretical studies of MoTe₂-MoSe₂ heterobilayers with rigid moiré superlattices controlled by the twist angle. Using an effective continuum model that combines resonant interlayer electron tunneling with stacking-dependent moiré potentials, we identify the nature of moiré excitons and the dependence of their energies, oscillator strengths and Landé g -factors on the twist angle. Within the same framework, we interpret distinct signatures of bound complexes among electrons and moiré excitons in nearly collinear heterostacks. Our work provides fundamental understanding of hybrid moiré excitons and trions in MoTe₂-MoSe₂ heterobilayers, and establishes the material system as a prime candidate for optical studies of correlated phenomena in moiré lattices.

In semiconducting transition metal dichalcogenide (TMD) heterostructures, electrons and holes located in distinct layers are bound by strong Coulomb attraction, forming interlayer excitons [1]. In contrast to intralayer excitons confined within one TMD layer, interlayer excitons are much longer-lived, exhibiting radiative lifetimes in the nanosecond range and facilitating long-range exciton- and valley-spin transport [2, 3]. In addition, the permanent out-of-plane electric dipole enables wide spectral tunability through the quantum-confined Stark effect [4, 5]. More recently, interlayer excitons in TMD moiré heterostructures have been employed to probe correlated electronic states [6, 7], and have been observed to form bosonic correlated states [8, 9].

Due to their spatially indirect nature, however, interlayer excitons in TMD heterostructures have more reduced electron-hole wave function overlap [10], which results in a negligible oscillator strength and thus substantially limits their coupling to light. One strategy to increase light-matter coupling of interlayer excitons relies on admixing of bright intralayer excitons through tunneling of electrons or holes in near-resonant moiré homobilayers and heterostructures. Related examples include MoS₂ and WSe₂ homobilayers [11, 12] as well as MoSe₂-WS₂ [13, 14] and MoSe₂-hBN-MoSe₂ [15] heterostructures. In MoSe₂-WS₂ heterobilayers, in particular, near-resonant conduction bands enhance the hybridization among interlayer and intralayer excitons and give rise to a multiplicity of moiré excitons with sizable oscillator strength [14]. This, in turn, provides all-optical means to probe the physics of correlated charges in moiré

lattices [15, 16].

In this work, we demonstrate that MoTe₂-MoSe₂ heterobilayers realize canonical moiré systems with near-resonant conduction bands. The large mismatch of $\sim 7\%$ between the lattice constants of MoTe₂ and MoSe₂ layers renders the system robust against mesoscopic lattice reconstruction [18], thus supporting moiré interference phenomena down to collinear alignment in parallel (R-type) and antiparallel (H-type) limits. The theoretically predicted conduction band offset of 38 meV is very small as compared to hundreds of meV in MoSe₂-WSe₂ and MoS₂-WSe₂ heterostacks [17]. We demonstrate that this small offset promotes sizable hybridization between interlayer (IX) and intralayer excitons (X) that share the hole state in the MoTe₂ layer and form moiré excitons [19] with high sensitivity to the twist angle of the MoTe₂-MoSe₂ heterostack. Moreover, we provide a theoretical framework that captures the main optical signatures of moiré excitons and their charged counterparts induced by field-effect doping.

The samples based on MoTe₂-MoSe₂ heterobilayers with different twist angles θ were stacked from exfoliated monolayers and encapsulated in thin hexagonal boron nitride (hBN) to ensure spectrally narrow exciton resonances [20]. For field-effect doping, the heterostacks were connected to a charge reservoir, and a few-layer graphite bottom gate was used to control the doping level via the gate voltage. Details of sample fabrication and determination of the twist angle θ are provided in Supplementary Note 1 and 4. Figure 1(b) shows the optical micrograph of a representative sample, with very clean

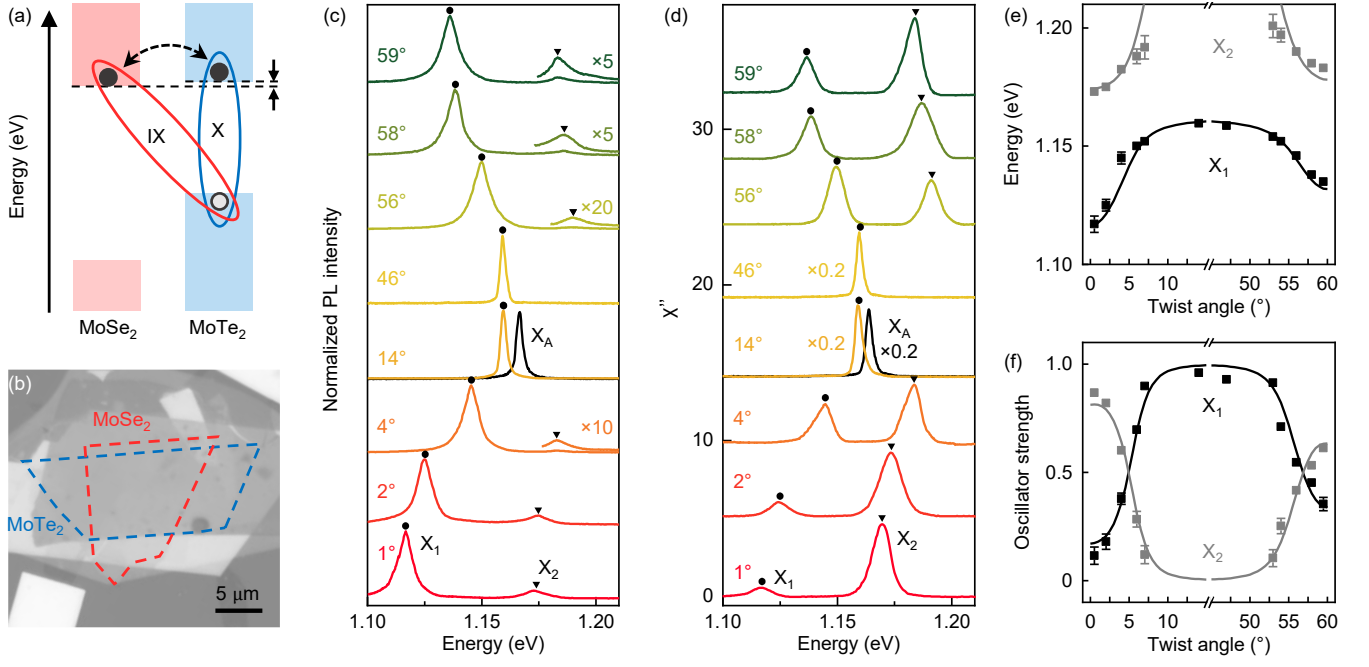


FIG. 1. (a) Schematic band diagram of MoTe₂-MoSe₂ in type-II band alignment with near-degenerate conduction band edges. The dashed arrow indicates resonant interlayer electron tunneling, which promotes the hybridization between interlayer exciton IX and intralayer exciton X states of MoTe₂. (b) Optical micrograph of a representative hBN-encapsulated heterobilayer with a twist angle of 58°. The edges of monolayer MoTe₂ and MoSe₂ are marked with dashed lines. (c) and (d) Normalized PL and absorption spectra (calculated as imaginary susceptibility χ'' from differential reflectivity via Kramers-Kronig transform), respectively, for heterobilayers with various twist angles at charge neutrality. Two characteristic peaks, X₁ and X₂, are highlighted by black dots and triangles, respectively. In both panels, single-peak spectra of monolayer MoTe₂ exciton X_A are shown in black lines. (e) and (f) Evolution of energy and oscillator strength for the peaks X₁ and X₂ as a function of the twist angle, respectively. The oscillator strength was obtained as the integrated peak area in absorption normalized to the peak area of X_A in monolayer MoTe₂. In both panels, the results of an effective moiré model (solid lines) fitted to the data (squares) yield the hopping parameter $t = 12$ meV and the energy difference between the decoupled X and IX exciton states as 54 meV, consistent with the *ab initio* conduction band offset of 38 meV [17].

interfaces between different layers. Owing to the large lattice mismatch, the heterostacks are rigidly locked in the canonical moiré geometry. Consistently, the spectral features in absorption and photoluminescence (PL) are very homogeneous across each MoTe₂-MoSe₂ sample (see Supplementary Note 5) without sizable variations.

Representative cryogenic PL and absorption spectra of MoTe₂-MoSe₂ heterobilayers at 3.2 K are shown in Fig. 1(c) and (d). For heterobilayers close to parallel R-type alignment ($\theta = 1^\circ, 2^\circ$ and 4°) and antiparallel H-type alignment ($\theta = 56^\circ, 58^\circ$ and 59°), the PL spectra feature two peaks, X₁ and X₂, located respectively at the low- and high-energy side of the A-exciton resonance of monolayer MoTe₂ at 1.168 eV labelled as X_A [21–24]. As shown in Fig. 1d, both peaks contribute to absorption with a spectral weight that depends on the twist angle. The peaks arise from angle-dependent hybridization of pure inter- and intralayer states, with admixed moiré excitons acquiring their oscillator strength from the fundamental exciton X_A of monolayer MoTe₂. Contrastingly, for the largely misaligned heterostacks ($\theta = 14^\circ$ and 46°), the PL and absorption spectra exhibit only one single peak with oscillator strength and energy similar to the

monolayer X_A exciton. This is consistent with a fully decoupled intralayer exciton in the heterostack, where the small energy red-shift from the X_A transitions is due to Coulomb screening by the adjacent MoSe₂ layer [25]. In addition to the stark differences between nearly aligned and largely twisted heterobilayers, the spectral features exhibit a continuous evolution with the twist angle, as evident from the data in Fig. 1(e) and (f). The trend is similar in R- and H-type stacks: both X₁ and X₂ feature peak energy minima in Fig. 1(e) for near-collinear alignments at $\theta \approx 0^\circ$ and 60° , where the absorption strength in Fig. 1(f) is minimal for X₁ and maximal for X₂. For increasing twist angles, the peak energies of both states increase continuously, and the oscillator strength is gradually transferred from X₂ to X₁. For angles above 7° (below 53°), the contribution of X₂ to both PL and absorption vanishes, whereas X₁ evolves into a state of pure intralayer character with almost constant absorption strength and transition energy for $7^\circ < \theta < 53^\circ$. Note that this evolution of the oscillator strength with the twist angle also manifests in the exciton recombination dynamics, with the lifetime of X₁ reducing continuously from several hundreds of ps in nearly collinear

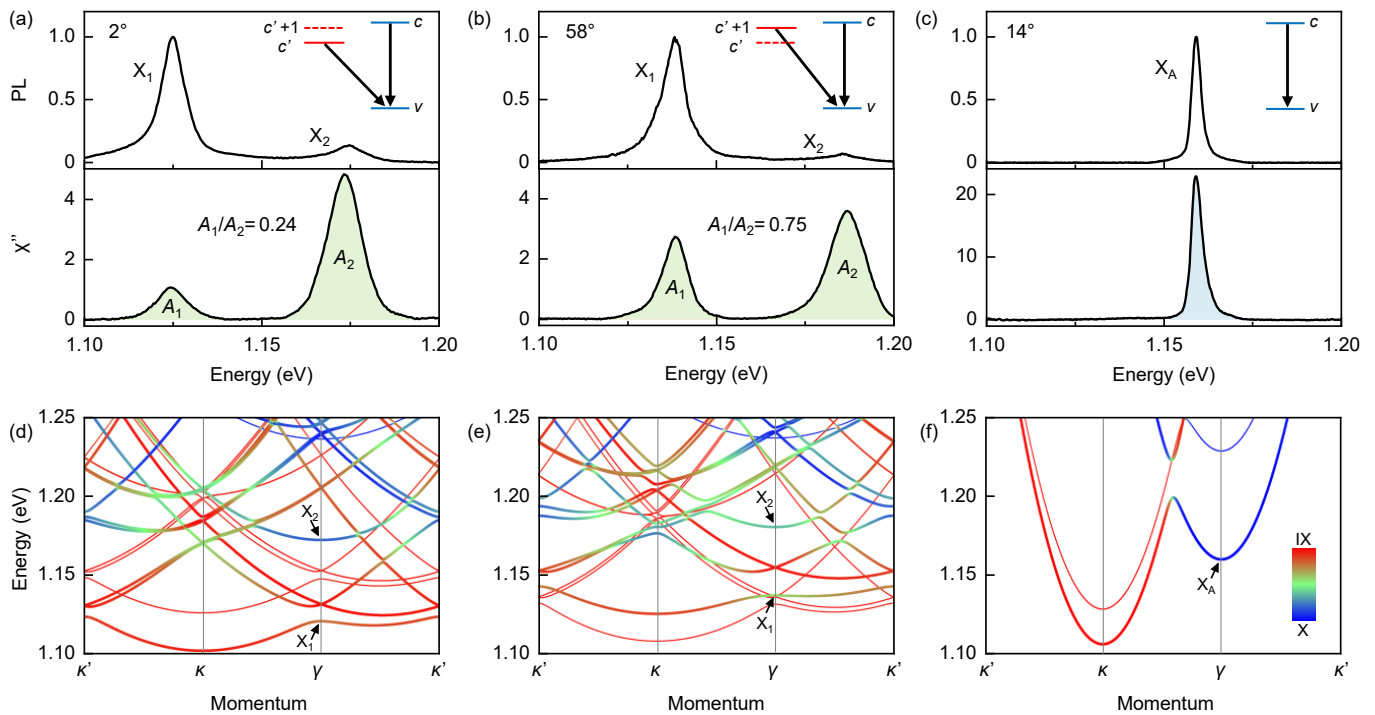


FIG. 2. (a–c) PL (upper panels) and absorption (lower panels) spectra of heterobilayers with 2° (a), 58° (b) and 14° (c) twist angles. Note that the absorption strength ratio (A_1/A_2) between X_1 and X_2 in stacks with 2° and 58° twist is very different despite the same rotation angle away from collinear alignment. For each twist angle, the inset illustrates the spin-polarized bands of MoSe₂ (red) and MoTe₂ (blue), with solid and dashed lines represent spin-up and spin-down polarized bands and the arrows indicate optical transitions involving spin-singlet excitons. (d–f) Calculated exciton dispersions in the mini Brillouin zone for twisted heterobilayers with twist angles as in (a–c). The color code in the inset of (f) represents the state composition, ranging from pure intralayer exciton X (blue) to pure interlayer exciton IX (red) character. Thick and thin lines represent singlet and triplet branches, and the arrows in each panel indicate the moiré states X_1 and X_2 with zero center-of-mass momentum involved in optical transitions.

heterostacks to less than 10 ps in largely twisted ones ($7^\circ < \theta < 53^\circ$), shown in Supplementary Note 6.

Despite the overall similar trends, it is instructive to note that R- and H-type stacks exhibit important dissimilarities when the angle deviation from ideal alignment is the same. As exemplified in Fig. 2(a) and (b) for heterostacks with 2° and 58° twist, respectively, the moiré peak doublets are red-shifted by ~ 13 meV with respect to each other, with X_1 and X_2 at 1.125 and 1.175 eV in Fig. 2(a) and 1.138 and 1.187 eV in Fig. 2(b). Moreover, the absorption strength ratio (A_1/A_2) of the moiré peaks X_1 and X_2 is about three times smaller for near-parallel alignment ($A_1/A_2 = 0.24$) as compared to the near-antiparallel alignment ($A_1/A_2 = 0.75$). Such differences in peak energies and absorption strength ratios are also evident in Fig. 1(e) and (f) for stacks with 1° and 59° as well as 4° and 56° twist angles.

To explain this set of spectral features and their evolution with the twist angle, we employed the phenomenological model of near-resonant hybridization in moiré heterostructures [14] (see Supplementary Note 8 for details). In brief, the model has two main contributions. First, the real-space moiré pattern is accounted for in the framework of the continuum model [26], where har-

monic expansion yields a complex moiré potential $V = |V| \exp(i\phi)$ with depth $|V|$ and phase ϕ characteristic of a given heterostructure and stacking type. Second, interlayer hybridization gives rise to electron Bragg scattering and the formation of a mini Brillouin zone [27], with high symmetry points γ and κ corresponding to the Brillouin zone corners of MoTe₂ and MoSe₂ monolayers, respectively. Interlayer tunnel coupling mixes the near-resonant conduction bands of MoTe₂ and MoSe₂ through electron hopping with parameter t , which gives rise to hybridization of intralayer and interlayer excitons X and IX with holes in the MoTe₂ layer and the respective energies $E_X = E_0$ and $E_{IX} = E_0 + \Delta$, where Δ quantifies the difference between the energy of IX excitons and the energy E_0 of the fundamental A-exciton in MoTe₂. To a first approximation [28], t is treated as a constant inside the mini Brillouin zone, and only spin-conserving electron tunneling can take place, involving different spin-split conduction bands of MoSe₂ in the hybridization of R- and H-type limits. We also assume that the twist angle has a negligible impact on the interlayer distances, local atomic arrangement, hopping parameters and moiré potential amplitude.

The results of the combined effective model are shown

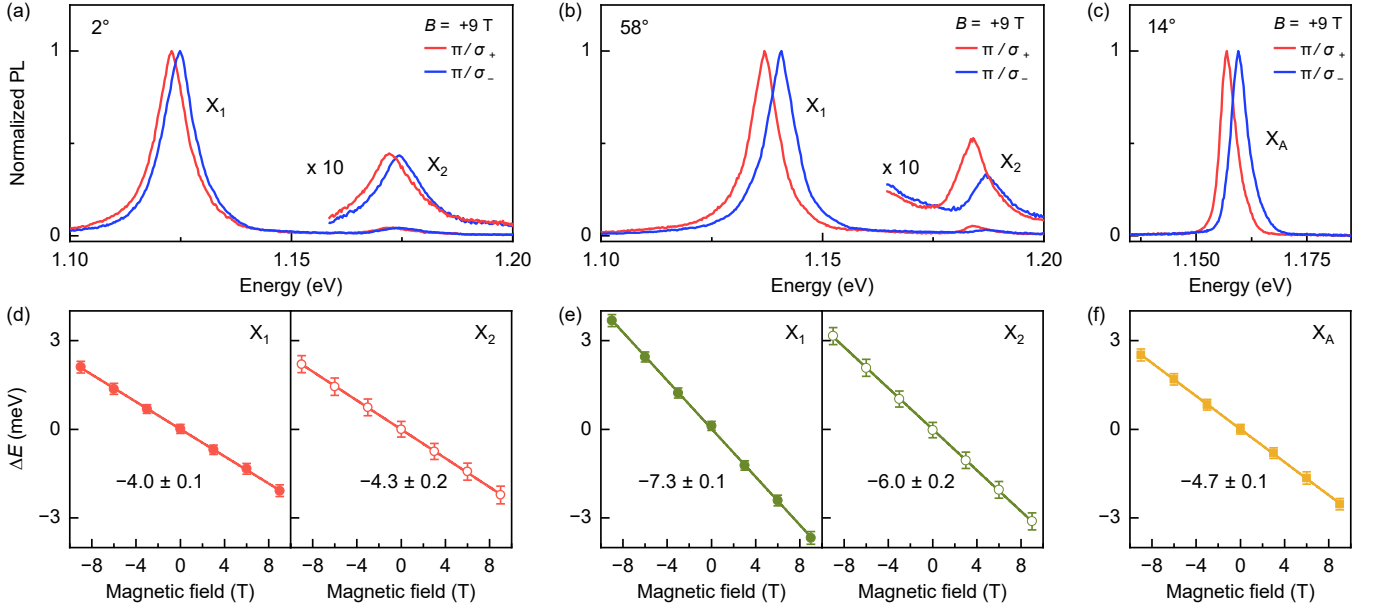


FIG. 3. Magneto-luminescence spectroscopy of heterobilayers with 2° , 58° and 14° twist angles. (a–c) PL spectra in perpendicular magnetic field of 9 T recorded with linearly polarized excitation (π) and circularly polarized detection (σ_+ and σ_-). For energies above 1.16 eV, spectra scaled by a factor of 10 in intensity were also included in (a) and (b) for clarity. (d–f) Zeeman splitting ΔE of the exciton peaks in (a–c) as a function of the magnetic field. The error bars originate from Voigt fits to the spectra. The respective exciton g -factors with least-square errors are extracted from linear fits (solid lines) and explicitly given in each panel.

as moiré exciton dispersions in Fig. 2(d)–(f) for three different cases, corresponding to the heterostacks with PL and absorption spectra in Fig. 2(a)–(c), respectively. Thick and thin lines represent spin singlet and triplet bands, and the arrows highlight the two optically active singlet moiré exciton states located at the γ point of the mini Brillouin zone due to hole-localization in the MoTe_2 layer. These two states correspond to bright moiré excitons with zero center-of-mass momentum and dipole-allowed direct optical transitions. All other states at γ are dark, as their admixing with the bright fundamental A-exciton of MoTe_2 is inhibited by symmetry. The color scale inset of Fig. 2(f) indicates the relative contributions of X and IX excitons to the bands.

The moiré exciton band structures in Fig. 2(d)–(f) are shown for best-fit parameters $E_0 = 1162$ meV, $\Delta = -54$ meV, $t = 12$ meV, and $|V| = 1$ meV, with stacking-dependent phases $\phi = 3\pi/4$ and $7\pi/12$ for R- and H-type limits. The values were obtained from best correspondence between twist-dependent energies and oscillator strengths of moiré states X_1 and X_2 in our simulations and experiments shown by the solid lines in Fig. 1(e) and (f) (see Supplementary Note 8 for details), taking into account the response of moiré excitons to electron doping discussed further below. Our model provides an intuition for the evolution of the energies and oscillator strength of both moiré peaks: the energy shifts of X_1 and X_2 stem from angle-dependent hybridization between X and IX excitons, which in turn redistributes the oscillator strength of the A-exciton in MoTe_2 among the hybrid

moiré states.

With this intuition, we understand the single optically active state in the spectra of largely twisted stacks as in Fig. 2(c) as an almost pure A-exciton of MoTe_2 , and the presence of two bright states in the spectra of nearly collinear stacks in Fig. 2(a) and (b) with $\theta = 2^\circ$ and 58° , respectively, as layer-hybridized moiré states with relatively flat dispersion and large effective masses. We also note that the admixing of IX and X exciton states is different for moiré excitons X_1 and X_2 for same angle deviations from ideal R- and H-alignments, e.g. as for $\theta = 2^\circ$ and 58° in Fig. 2. This difference is due to the reversed spin-ordering of decoupled IX bands in R- and H-type heterobilayers, rendering both the energy and the oscillator strength of hybrid moiré excitons asymmetric for angles close to 0° and 60° , as in Fig. 1(e) and (f).

Magneto-luminescence studies provide further quantitative support for our analysis. From magneto-dispersed polarization-contrasting PL spectra as in Fig. 3(a)–(c) at 9 T, recorded for heterobilayers with $\theta = 2^\circ$, 58° , and 14° twist angle, respectively, we deduce the characteristic g -factors of moiré exciton peaks. The corresponding Zeeman splittings ΔE , given by the energy difference between the maxima of σ_+ and σ_- polarized peaks, are shown in Fig. 3(d)–(f) as a function of the magnetic field B applied perpendicularly to the heterostack. Linear fits to the data with $\Delta E = g\mu_B B$ and the Bohr magneton μ_B , yield the exciton g -factors of -4.7 ± 0.1 for X_A in the heterostructure with 14° twist, as well as -4.0 ± 0.1 and -4.3 ± 0.2 and -7.3 ± 0.1 and -6.0 ± 0.2 for X_1 and X_2

moiré peaks in heterostacks with 2° and 58° twist angles, respectively. The g -factor of the single peak X_A in the spectra of stacks with large twist angles is within error bars identical to the value of the fundamental exciton in monolayer MoTe_2 , determined as -4.6 ± 0.1 (see Supplementary Fig. S1), whereas the g -factors of both moiré peaks in nearly collinear stacks are distinct.

We employed *ab initio* calculations for theoretical estimates of the exciton g -factor in monolayer MoTe_2 and moiré excitons in MoTe_2 - MoSe_2 heterostructures [29–32]. For the fundamental exciton X_A in monolayer MoTe_2 , we obtained $g_A = -4.6$ from:

$$g_A = 2(L_c - L_v), \quad (1)$$

with the orbital angular momenta of the lowest conduction band and the highest valence band L_c and L_v . For moiré excitons, we decompose the g -factors into the individual contributions of interlayer and intralayer excitons [33] according to hybridization-induced admixing as:

$$g_i^{(R)} = 2 \left(f_i^{(X)} L_c + f_i^{(IX)} L_{c'} - L_v \right), \quad (2)$$

$$g_i^{(H)} = 2 \left(f_i^{(X)} L_c - f_i^{(IX)} L_{c'+1} - L_v \right), \quad (3)$$

where $i = 1, 2$ indicates the hybrid X_i exciton, $L_{c'(c'+1)}$ is the first (second) conduction band in MoSe_2 layer as shown in the insets of Fig. 2(a) and (b), and $f_i^{(X)}$ ($f_i^{(IX)}$) is the fraction of X (IX) exciton. Using the calculated values of the orbital angular momenta in Table S2 and the respective exciton fractions deduced from our effective model, we obtain $g_1^{(R)} = -4.2$ and $g_2^{(R)} = -4.4$ for X_1 and X_2 moiré excitons in heterostacks with 2° twist, as well as $g_1^{(H)} = -8.0$ and $g_2^{(H)} = -6.8$ in stacks with 58° twist angle. The overall agreement between the theoretical and experimental g -factor values provides strong confidence in our understanding of the intralayer and interlayer exciton character of moiré excitons X_1 and X_2 . The small discrepancies between the theoretical and experimental values are not surprising given the finite extent of excitons in momentum space, with contributions of different orbital angular momentum values away from the K point [14] unaccounted for in our model.

Remarkably, the decomposition of moiré excitons into their respective intralayer and interlayer exciton fractions is the key to the understanding of the distinct behaviors observed upon electron doping in Fig. 4(a) and (b) for stacks with 2° and 58° twist angles. In the PL of the stack close to R-type alignment in Fig. 4(a), electron doping at elevated positive gate voltages induces a trion or attractive Fermi-polaron feature X_1^- red-shifted by 14 meV from the moiré peak X_1 , whereas the peak X_2 remains almost unaffected. The PL of the stack near H-type alignment in Fig. 4(b), on the other hand, exhibits the signature of the bound charge complex X_2^- with a binding energy of 18 meV, with X_1 being merely affected by doping. This contrasting response to electron doping in R- and H-type stacks, where at low doping electrons occupy

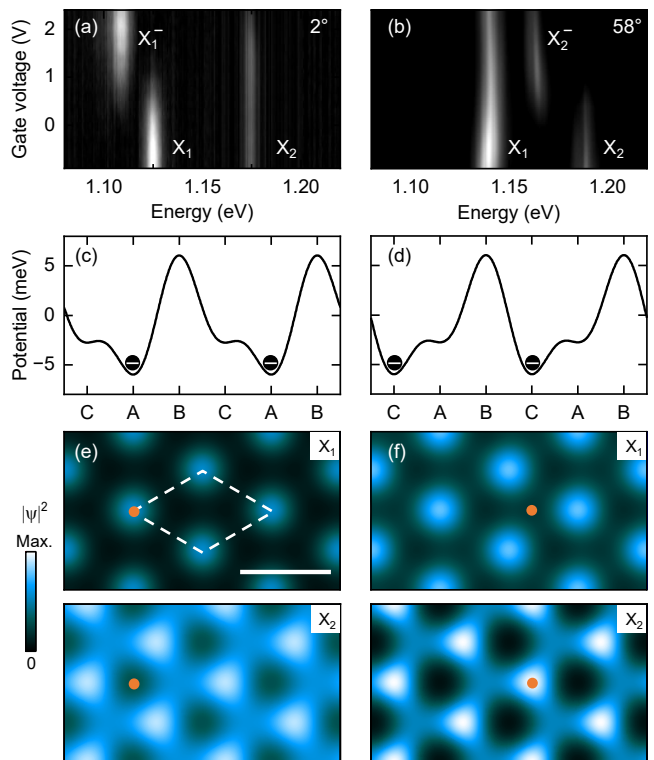


FIG. 4. Hybrid moiré triions in MoTe_2 - MoSe_2 heterostacks. (a) and (b) PL evolution with electron doping induced by the gate voltage in heterostacks with twist angles of 2° and 58° , respectively. (c) and (d) Moiré potential for electrons in MoTe_2 across the high-symmetry stacking sites A, B, and C of the moiré unit cell shown in (e) by the dashed line (scale bar: 5 nm). (e) and (f) Color-coded maps of real-space probability functions $|\psi|^2$ of intralayer excitons contributing to X_1 (upper panel) and X_2 (lower panel) excitons. Orange dots indicate in each panel one representative electron-localizing site at low doping levels.

the MoTe_2 layer first due to its lower conduction band edge, stems from both different hybridization characters of moiré excitons and distinct spatial positions of field-induced electrons inside the moiré unit cell [14, 34, 35].

To highlight these differences, we plot the moiré potential for electrons across the unit cell for nearly collinear heterostacks with $\theta = 2^\circ$ and 58° in Fig. 4 (c) and (d), respectively, and in Fig. 4 (e) and (f) the spatial distributions of intralayer exciton wavefunctions contributing to X_1 (top panels) and X_2 (bottom panels) moiré excitons. Taking into account that electron-hole interactions are larger for intralayer charges than in their layer-separated limit [36], the localization of the hole in the MoTe_2 monolayer favors the formation of bound exciton-charge complexes for electrons that are spatially co-localized with the interlayer part of moiré excitons. In moiré unit cells of R-type heterostacks, this is the case at sites A, where the spatial contribution of the intralayer exciton wavefunction is maximal for X_1 and minimal for X_2 . In H-stacks, on the contrary, electrons localize at sites C

with minimal and maximal contribution of the electron-binding intralayer exciton to X_1 and X_2 . At low doping levels, spatial co-localization of moiré-trapped electrons with the intralayer exciton part of moiré excitons X_1 and X_2 thus determines the presence or absence of the corresponding trion states, with binding energies bound by the trion binding energy of ~ 22 meV in monolayer MoTe₂ [21–24, 37] due to finite admixing of interlayer character.

In summary, our combined experimental and theoretical study of MoTe₂-MoSe₂ heterostructures identifies the hybrid nature of moiré excitons as a function of twist angle. The optically active moiré states with resonances in absorption and emission are composed of admixtures of intralayer and interlayer excitons, with strong dependence of the respective fractional contributions on the twist angle. These fractions in turn determine the g -factors of moiré excitons, which we quantified in magneto-luminescence and in *ab initio* calculations. Moreover, these fractions condition distinct responses of H- and R-type heterostacks to electron doping at low doping levels, where electrons are spatially localized in stacking-specific points of the moiré supercell to form bound complexes with co-localized moiré excitons. The high degree of intralayer-interlayer hybridization of moiré excitons in MoTe₂-MoSe₂ heterobilayers with near-resonant conduction band alignment, along with their optical signatures of charge carrier doping, establish the system as a versatile material platform for future studies of moiré correlated quantum phenomena.

Associated Content

Supporting Information: Details on sample fabrication, optical spectroscopy methods, optical spectroscopy of monolayers, determination of heterobilayer twist angles, sample homogeneity, photoluminescence decay of hybrid excitons, excitation power dependence of hybrid excitons, theoretical model of exciton hybridization, dependence of hybrid excitons on twist angle and density functional theory.

Author Information

Corresponding authors:

X. H. (xinhuang@iphy.ac.cn), A. H. (alexander.hoegele@lmu.de) and A. S. B. (anvar.baimuratov@lmu.de).

Author contributions:

S. Z. and X. H. contributed equally to this work.

Notes:

The authors declare no competing financial interest.

Acknowledgements: This research was funded by the European Research Council (ERC) under the Grant Agreement No. 772195 as well as the Deutsche Forschungsgemeinschaft (DFG, German Research Foundation) within the Priority Programme SPP 2244 2DMP and the Germany’s Excellence Strategy EXC-2111-390814868 (MCQST). S. Z. acknowledges support from the Alexander von Humboldt Foundation. X. H. acknowledges the National Natural Science Foundation of China

(grant No. 62204259). R. G. and J. M. acknowledge the scientific support and HPC resources provided by the Erlangen National High Performance Computing Center (NHR@FAU) of the Friedrich-Alexander-Universität Erlangen-Nürnberg (FAU); the hardware was funded by the German Research Foundation (DFG), grant No. 440719683. Z. L. was supported by the China Scholarship Council (grant No. 201808140196). S. L. and J. H. were supported by the Columbia University Materials Science and Engineering Research Center (MRSEC), through NSF grants DMR-1420634 and DMR-2011738. K. W. and T. T. acknowledge support from the JSPS KAKENHI (Grant Numbers 20H00354 and 23H02052) and World Premier International Research Center Initiative (WPI), MEXT, Japan. A. S. B. acknowledges funding by the European Union’s Framework Programme for Research and Innovation Horizon 2020 under the Marie Skłodowska-Curie grant agreement No. 754388 (LMUResearchFellows) and from LMUexcellent, funded by the Federal Ministry of Education and Research (BMBF) and the Free State of Bavaria under the Excellence Strategy of the German Federal Government and the Länder. A. H. acknowledges funding by the Bavarian Hightech Agenda within the EQAP project.

References

- [1] P. Rivera, H. Yu, K. L. Seyler, N. P. Wilson, W. Yao, and X. Xu, Interlayer valley excitons in heterobilayers of transition metal dichalcogenides, *Nat. Nanotechnol.* **13**, 1004 (2018).
- [2] C. Jin, J. Kim, M. I. B. Utama, E. C. Regan, H. Kleemann, H. Cai, Y. Shen, M. J. Shinner, A. Sengupta, K. Watanabe, T. Taniguchi, S. Tongay, A. Zettl, and F. Wang, Imaging of pure spin-valley diffusion current in WS₂-WSe₂ heterostructures, *Science* **360**, 893 (2018).
- [3] D. Unuchek, A. Ciarrocchi, A. Avsar, K. Watanabe, T. Taniguchi, and A. Kis, Room-temperature electrical control of exciton flux in a van der Waals heterostructure, *Nature* **560**, 340 (2018).
- [4] L. A. Jauregui, A. Y. Joe, K. Pistunova, D. S. Wild, A. A. High, Y. Zhou, G. Scuri, K. De Greve, A. Sushko, C.-H. Yu, T. Taniguchi, K. Watanabe, D. J. Needleman, M. D. Lukin, H. Park, and P. Kim, Electrical control of interlayer exciton dynamics in atomically thin heterostructures, *Science* **366**, 870 (2019).
- [5] A. Ciarrocchi, D. Unuchek, A. Avsar, K. Watanabe, T. Taniguchi, and A. Kis, Polarization switching and electrical control of interlayer excitons in two-dimensional van der Waals heterostructures, *Nat. Photon.* **13**, 131 (2019).
- [6] S. Miao, T. Wang, X. Huang, D. Chen, Z. Lian, C. Wang, M. Blei, T. Taniguchi, K. Watanabe, S. Tongay, Z. Wang, D. Xiao, Y.-T. Cui, and S.-F. Shi, Strong interaction between interlayer excitons and correlated electrons in WSe₂/WS₂ moiré superlattice, *Nat. Commun.* **12**, 3608 (2021).
- [7] Q. Tan, A. Rasmita, Z. Zhang, H. Cai, X. Cai, X. Dai, K. Watanabe, T. Taniguchi, A. H. MacDonald, and W. Gao, Layer-dependent correlated phases

- in WSe₂/MoS₂ moiré superlattice, *Nat. Mater.* **22**, 605 (2023).
- [8] H. Park, J. Zhu, X. Wang, Y. Wang, W. Holtzmann, T. Taniguchi, K. Watanabe, J. Yan, L. Fu, T. Cao, D. Xiao, D. R. Gamelin, H. Yu, W. Yao, and X. Xu, Dipole ladders with large Hubbard interaction in a moiré exciton lattice, *Nat. Phys.* **19**, 1286 (2023).
- [9] Z. Lian, Y. Meng, L. Ma, I. Maity, L. Yan, Q. Wu, X. Huang, D. Chen, X. Chen, X. Chen, M. Blei, T. Taniguchi, K. Watanabe, S. Tongay, J. Lischner, Y.-T. Cui, and S.-F. Shi, Valley-polarized excitonic mott insulator in WS₂/WSe₂ moiré superlattice, *Nat. Phys.* **20**, 34 (2024).
- [10] R. Gillen and J. Maultzsch, Interlayer excitons in MoSe₂/WSe₂ heterostructures from first principles, *Phys. Rev. B* **97**, 165306 (2018).
- [11] N. Leisgang, S. Shree, I. Paradisanos, L. Sponfeldner, C. Robert, D. Lagarde, A. Balocchi, K. Watanabe, T. Taniguchi, X. Marie, R. J. Warburton, I. C. Gerber, and B. Urbaszek, Giant Stark splitting of an exciton in bilayer MoS₂, *Nat. Nanotechnol.* **15**, 901 (2020).
- [12] F. Tagarelli, E. Lopriore, D. Erckensten, R. Perea-Causín, S. Brem, J. Hagel, Z. Sun, G. Pasquale, K. Watanabe, T. Taniguchi, E. Malic, and A. Kis, Electrical control of hybrid exciton transport in a van der Waals heterostructure, *Nat. Photon.* **17**, 615 (2023).
- [13] Y. Tang, J. Gu, S. Liu, K. Watanabe, T. Taniguchi, J. Hone, K. F. Mak, and J. Shan, Tuning layer-hybridized moiré excitons by the quantum-confined Stark effect, *Nat. Nanotechnol.* **16**, 52 (2021).
- [14] B. Polovnikov, J. Scherzer, S. Misra, X. Huang, C. Mohl, Z. Li, J. Göser, J. Förste, I. Bilgin, K. Watanabe, T. Taniguchi, A. Högele, and A. S. Baimuratov, Field-induced hybridization of moiré excitons in MoSe₂/WS₂ heterobilayers, *Phys. Rev. Lett.* **132**, 076902 (2024).
- [15] Y. Shimazaki, I. Schwartz, K. Watanabe, T. Taniguchi, M. Kroner, and A. Imamoğlu, Strongly correlated electrons and hybrid excitons in a moiré heterostructure, *Nature* **580**, 472 (2020).
- [16] L. Ciorciaro, T. Smoleński, I. Morera, N. Kiper, S. Hiesland, M. Kroner, Y. Zhang, K. Watanabe, T. Taniguchi, E. Demler, and A. Imamoğlu, Kinetic magnetism in triangular moiré materials, *Nature* **623**, 509 (2023).
- [17] C. Zhang, C. Gong, Y. Nie, K.-A. Min, C. Liang, Y. J. Oh, H. Zhang, W. Wang, S. Hong, L. Colombo, R. M. Wallace, and K. Cho, Systematic study of electronic structure and band alignment of monolayer transition metal dichalcogenides in van der Waals heterostructures, *2D Mater.* **4**, 015026 (2016).
- [18] S. Zhao, Z. Li, X. Huang, A. Rupp, J. Göser, I. A. Vovk, S. Y. Kruchinin, K. Watanabe, T. Taniguchi, I. Bilgin, A. S. Baimuratov, and A. Högele, Excitons in mesoscopically reconstructed moiré heterostructures, *Nat. Nanotechnol.* **18**, 572 (2023).
- [19] T. Deilmann and K. S. Thygesen, Interlayer excitons with large optical amplitudes in layered van der Waals materials, *Nano Lett.* **18**, 2984 (2018).
- [20] F. Cadiz, E. Courtade, C. Robert, G. Wang, Y. Shen, H. Cai, T. Taniguchi, K. Watanabe, H. Carrere, D. Lagarde, M. Manca, T. Amand, P. Renucci, S. Tongay, X. Marie, and B. Urbaszek, Excitonic linewidth approaching the homogeneous limit in MoS₂-based van der Waals heterostructures, *Phys. Rev. X* **7**, 021026 (2017).
- [21] C. Ruppert, B. Aslan, and T. F. Heinz, Optical properties and band gap of single- and few-layer MoTe₂ crystals, *Nano Lett.* **14**, 6231 (2014).
- [22] I. G. Lezama, A. Arora, A. Ubaldini, C. Barreteau, E. Giannini, M. Potemski, and A. F. Morpurgo, Indirect-to-direct band gap crossover in few-layer MoTe₂, *Nano Lett.* **15**, 2336 (2015).
- [23] G. Froehlicher, E. Lorchat, and S. Berciaud, Direct versus indirect band gap emission and exciton-exciton annihilation in atomically thin molybdenum ditelluride (MoTe₂), *Phys. Rev. B* **94**, 085429 (2016).
- [24] C. Robert, R. Picard, D. Lagarde, G. Wang, J. P. Echeverry, F. Cadiz, P. Renucci, A. Högele, T. Amand, X. Marie, I. C. Gerber, and B. Urbaszek, Excitonic properties of semiconducting monolayer and bilayer MoTe₂, *Phys. Rev. B* **94**, 155425 (2016).
- [25] A. Raja, A. Chaves, J. Yu, G. Arefe, H. M. Hill, A. F. Rigosi, T. C. Berkelbach, P. Nagler, C. Schüller, T. Korn, C. Nuckolls, J. Hone, L. E. Brus, T. F. Heinz, D. R. Reichman, and A. Chernikov, Coulomb engineering of the bandgap and excitons in two-dimensional materials, *Nat. Commun.* **8**, 15251 (2017).
- [26] F. Wu, T. Lovorn, and A. H. MacDonald, Topological Exciton Bands in Moiré Heterojunctions, *Phys. Rev. Lett.* **118**, 147401 (2017).
- [27] D. A. Ruiz-Tijerina and V. I. Fal'ko, Interlayer hybridization and moiré superlattice minibands for electrons and excitons in heterobilayers of transition-metal dichalcogenides, *Phys. Rev. B* **99**, 125424 (2019).
- [28] Y. Wang, Z. Wang, W. Yao, G.-B. Liu, and H. Yu, Interlayer coupling in commensurate and incommensurate bilayer structures of transition-metal dichalcogenides, *Phys. Rev. B* **95**, 115429 (2017).
- [29] J. Förste, N. V. Tepliakov, S. Yu. Kruchinin, J. Lindlau, V. Funk, M. Förg, K. Watanabe, T. Taniguchi, A. S. Baimuratov, and A. Högele, Exciton *g*-factors in monolayer and bilayer WSe₂ from experiment and theory, *Nat. Commun.* **11**, 4539 (2020).
- [30] T. Deilmann, P. Krüger, and M. Rohlfing, Ab initio studies of exciton *g* factors: Monolayer transition metal dichalcogenides in magnetic fields, *Phys. Rev. Lett.* **124**, 226402 (2020).
- [31] T. Woźniak, P. E. Faria Junior, G. Seifert, A. Chaves, and J. Kunstmann, Exciton *g* factors of van der Waals heterostructures from first-principles calculations, *Phys. Rev. B* **101**, 235408 (2020).
- [32] M. Förg, A. S. Baimuratov, S. Yu. Kruchinin, I. A. Vovk, J. Scherzer, J. Förste, V. Funk, K. Watanabe, T. Taniguchi, and A. Högele, Moiré excitons in MoSe₂-WSe₂ heterobilayers and heterotrilayers, *Nat. Commun.* **12**, 1 (2021).
- [33] P. E. Faria Junior and J. Fabian, Signatures of electric field and layer separation effects on the spin-valley physics of MoSe₂/WSe₂ heterobilayers: From energy bands to dipolar excitons, *Nanomaterials* **13** (2023).
- [34] C. Jin, E. C. Regan, A. Yan, M. Iqbal Bakti Utama, D. Wang, S. Zhao, Y. Qin, S. Yang, Z. Zheng, S. Shi, K. Watanabe, T. Taniguchi, S. Tongay, A. Zettl, and F. Wang, Observation of moiré excitons in WSe₂/WS₂ heterostructure superlattices, *Nature* **567**, 76 (2019).
- [35] M. H. Naik, E. C. Regan, Z. Zhang, Y.-H. Chan, Z. Li, D. Wang, Y. Yoon, C. S. Ong, W. Zhao, S. Zhao, M. I. B. Utama, B. Gao, X. Wei, M. Sayyad, K. Yumigeta, K. Watanabe, T. Taniguchi, S. Tongay, F. H. da Jornada, F. Wang, and S. G. Louie, Intralayer charge-

- transfer moiré excitons in van der Waals superlattices, *Nature* **609**, 52 (2022).
- [36] E. Liu, E. Barré, J. van Baren, M. Wilson, T. Taniguchi, K. Watanabe, Y.-T. Cui, N. M. Gabor, T. F. Heinz, Y.-C. Chang, and C. H. Lui, Signatures of moiré trions in WSe₂/MoSe₂ heterobilayers, *Nature* **594**, 46 (2021).
- [37] S. Biswas, A. Champagne, J. B. Haber, S. Pokawanvit, J. Wong, H. Akbari, S. Krylyuk, K. Watanabe, T. Taniguchi, A. V. Davydov, Z. Y. Al Balushi, D. Y. Qiu, F. H. da Jornada, J. B. Neaton, and H. A. Atwater, Rydberg excitons and trions in monolayer MoTe₂, *ACS Nano* **17**, 7685 (2023).

Supplemental Information for

Hybrid moiré excitons and trions in twisted MoTe₂-MoSe₂ heterobilayers

Shen Zhao^{1,‡}, Xin Huang^{2,3,1,*,‡}, Roland Gillen⁴, Zhijie Li¹, Song Liu⁵, Kenji Watanabe⁶, Takashi Taniguchi⁷, Janina Maultzsch⁴, James Hone⁵, Alexander Högele^{1,8,*} and Anvar S. Baimuratov^{1,*}

¹*Fakultät für Physik, Munich Quantum Center,
and Center for NanoScience (CeNS),
Ludwig-Maximilians-Universität München,*

Geschwister-Scholl-Platz 1, 80539 München, Germany

²*Beijing National Laboratory for Condensed Matter Physics, Institute of Physics,
Chinese Academy of Sciences and School of Physical Sciences,*

CAS Key Laboratory of Vacuum Physics,

University of Chinese Academy of Sciences, Beijing 100190, P. R. China

³*School of Physical Sciences, CAS Key Laboratory of Vacuum Physics,
University of Chinese Academy of Sciences, Beijing 100190, P. R. China*

⁴*Department of Physics, Friedrich-Alexander Universität Erlangen-Nürnberg,
Staudtstraße 7, 91058 Erlangen, Germany*

⁵*Department of Mechanical Engineering, Columbia University,
New York, New York 10027, United States*

⁶*Research Center for Electronic and Optical Materials,
National Institute for Materials Science,
1-1 Namiki, Tsukuba 305-0044, Japan*

⁷*Research Center for Materials Nanoarchitectonics,
National Institute for Materials Science,
1-1 Namiki, Tsukuba 305-0044, Japan and*

⁸*Munich Center for Quantum Science and Technology (MCQST),
Schellingstraße 4, 80799 München, Germany*

[‡] S. Z. and X. H. contributed equally to this work.

*X. H. (xinhuang@iphy.ac.cn), A. H. (alexander.hoegle@lmu.de), A. S. B. (anvar.baimuratov@lmu.de).

CONTENTS

Note 1: Sample fabrication	3
Note 2: Optical measurement methods	3
Note 3: Optical spectroscopy of monolayers	4
Note 4: Determination of heterobilayer twist angles	5
Note 5: Sample homogeneity	7
Note 6: Photoluminescence decay of hybrid excitons	8
Note 7: Excitation power dependence of hybrid excitons	11
Note 8: Theoretical model of exciton hybridization	12
Note 9: Dependence of hybrid excitons on twist angle	15
Note 10: Density functional theory	17
Supplementary References	18

Supplementary Note 1: Sample fabrication

Fully hexagonal boron nitride (hBN) encapsulated MoTe₂-MoSe₂ heterostructure devices were fabricated by a dry-transfer method [1]. First, monolayers of MoTe₂, MoSe₂, few layer graphite and thin flakes of hBN were mechanically exfoliated from their bulk crystals onto Si/SiO₂ substrates. MoTe₂ bulk crystals were synthesized using a two-step flux method [2] with a relatively low defect density ($< 10^{10} \text{ cm}^{-2}$). MoSe₂ and graphite bulk crystals were purchased from HQ graphene, while hBN crystals were provided by the National Institute for Materials Science (NIMS). In a second step, a PC/PDMS stamp was used to assemble atomically thin flakes layer-by-layer. The pick-up temperatures for hBN flakes, thin graphite layers and monolayers of MoTe₂ and MoSe₂ was 50 °C, 90 °C, 40 °C, and 50 °C, respectively. The entire heterostructure was subsequently released from the stamp onto a 285 nm Si/SiO₂ substrates with prepatterned Cr/Au (5 nm/40 nm) electrodes at 170 °C. Finally, the device was annealed in high vacuum (10^{-9} mbar) for 12 h at a temperature of 200 °C to remove polymer residuals and improve interlayer coupling [3]. After the fabrication, the stacking type and twist angle of each MoTe₂-MoSe₂ heterobilayer was determined by second harmonic generation measurements (see Supplementary Note 4).

Supplementary Note 2: Optical spectroscopy methods

All optical measurements were performed at 3.2 K using a home-built confocal microscope in back-scattering geometry. The samples were loaded into a closed-cycle cryostat (attocube systems, attoDRY1000) with magnetic field ranging from -9 T to $+9$ T in the Faraday configuration; xyz piezo-stepping and xy scanning units (attocube systems, ANPxyz and ANSxy100) were employed for sample positioning. An apochromatic cryogenic objective with a numerical aperture of 0.81 (attocube systems, LT-APO/IR/0.81) was used to confocally excite and collect the signal from sample with a spot size of $\sim 1 \mu\text{m}$. For photoluminescence (PL) measurements, the excitation source was a Ti:sapphire laser (Coherent, Mira) in continuous-wave mode. The laser was tuned to the $2s$ exciton resonance of monolayer MoTe₂ at 975 nm and the incident power was kept at $5 \mu\text{W}$ unless otherwise specified. For differential reflectivity (DR) measurements, a power-stabilized Tungsten-Halogen lamp (Thorlabs, SLS201L) was used as a broadband light source. The PL or reflection signal were spectrally dispersed by a monochromator (Roper Scientific, Acton SP2500 with a 300 grooves/mm

grating) and detected by a liquid nitrogen cooled charge-coupled device (Roper Scientific, Spec-10:100BR) or a one-dimensional linear InGaAs photodiode array (Roper Scientific, OMA V:1024-1.7 LN). The DR spectra were obtained by normalizing the reflected spectrum of the sample (R_s) to the reference spectrum from nearby region without MoTe₂ and MoSe₂ layers but having both hBN and graphite layers (R_r), as $DR = \Delta R/R = (R_s - R_r)/R_r$. The absorption χ'' spectra were then derived from DR by accounting for the interference of multiple thin-layer reflections [4, 5]. For magneto-PL measurements, a set of linear polarizers (Thorlabs, LPVIS), half- and quarter-waveplates (B. Halle, super-achromatic) mounted on piezo-rotators (attocube systems, ANR240) were used to control the polarization in excitation and detection. For time-resolved PL measurements, a supercontinuum laser (NKT Photonics, SuperK Extreme) with a pulse duration of 4 ps was coupled to an acousto-optic tunable filter (NKT Photonics, SuperK Select nIR1) for pulsed excitation at 975 nm. The PL signal was detected by a superconducting nanowire single-photon detector (Scontel, TCOPRS-CCR-SW-85) and the photon detection events were time-correlated with the trigger signal from the supercontinuum laser by a electronic correlator (PicoQuant, PicoHarp 300). The count rate was adjusted to $< 1\%$ of the laser rate to prevent pile-up effects. The instrument response function (IRF) was measured by detecting the laser pulse using the same setup, and the bi-exponential fitting of the PL decay with deconvoluted IRF were performed using EasyTau 2 software (Picoquant). To control charge carrier density, the voltage was applied to the graphite gate with a sourcemeter (Keithley 2400).

Supplementary Note 3: Optical spectroscopy of monolayers

Figure S1 displays the PL characteristics results of monolayer regions in an hBN-encapsulated device. For both MoTe₂ and MoSe₂, their typical PL spectra show bright and spectrally narrow A-exciton peaks. The corresponding full width at half maximum (FWHM) linewidths are 3.5 and 1.5 meV, respectively, approaching the homogeneous limit [6]. Moreover, the spectra have very weak trion features as compared to the A-exciton, which implies a low density of charge defects [7]. These results confirm high quality of the individual monolayers upon device fabrication. To compare the exciton g -factors between monolayer and heterobilayer, we performed magneto-photoluminescence measurements on the A-exciton of monolayer MoTe₂ and MoSe₂. The obtained g -factors are respectively -4.6 and -4.3 , in accord with previous reports [8, 9].

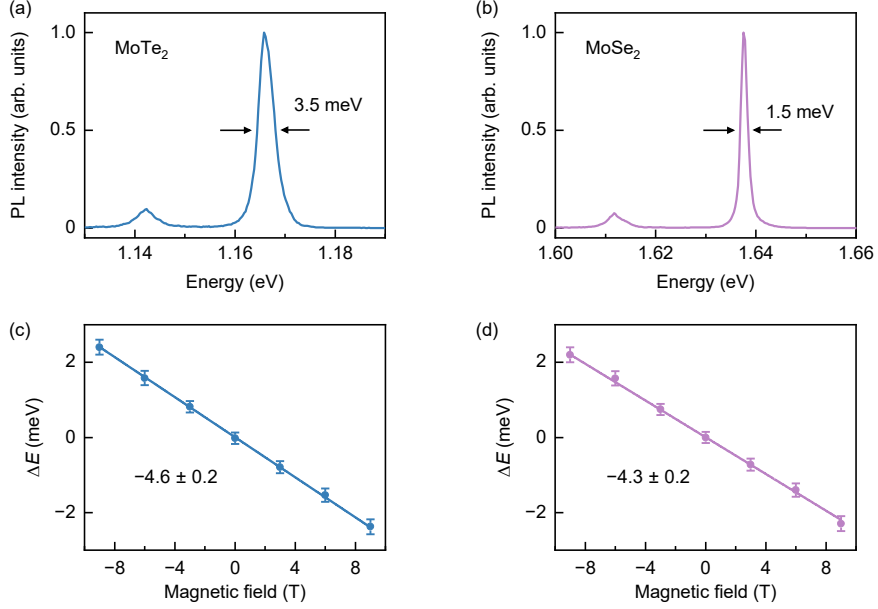


FIG. S1. PL characterization of MoTe₂ and MoSe₂ monolayers in a MoTe₂-MoSe₂ heterobilayer sample. (a) and (b) Typical PL spectra of MoTe₂ and MoSe₂ at zero gate voltage, showing narrow linewidth of the A-exciton transitions and weak emission from trions. (c) and (d) Zeeman splitting ΔE of MoTe₂ and MoSe₂ A-excitons as a function of the magnetic field. The corresponding g -factors are extracted from the slopes of linear fits shown by solid lines.

Supplementary Note 4: Determination of heterobilayer twist angles

To determine the relative twist angle between MoTe₂ and MoSe₂ layers, we performed polarization-resolved second harmonic generation (SHG) measurements at 3.2 K using a home-built system. A supercontinuum laser with 4 ps pulse duration and 80 MHz repetition rate was used to excite at 1280 nm below the optical bandgap of MoTe₂-MoSe₂ heterobilayer. For each measurement, the excitation laser with a power of 5 mW was linearly polarized and focused onto a $\sim 2 \mu\text{m}$ spot by an objective lens with a numerical aperture of 0.81. The SHG signal was collected by the same objective and separated from the reflected laser using a beam splitter and a short-pass filter. A linear polarizer was then placed in the SHG signal path and aligned parallel to the excitation polarization as analyzer. The angle resolution was realized by rotating a motorized half-wave plate located just above the objective. The SHG signal was finally recorded by a spectrometer with a 300 grooves/mm grating and a liquid-nitrogen-cooled charge-coupled device.

Given the six-fold rotational symmetry of monolayer transition metal dichalcogenides,

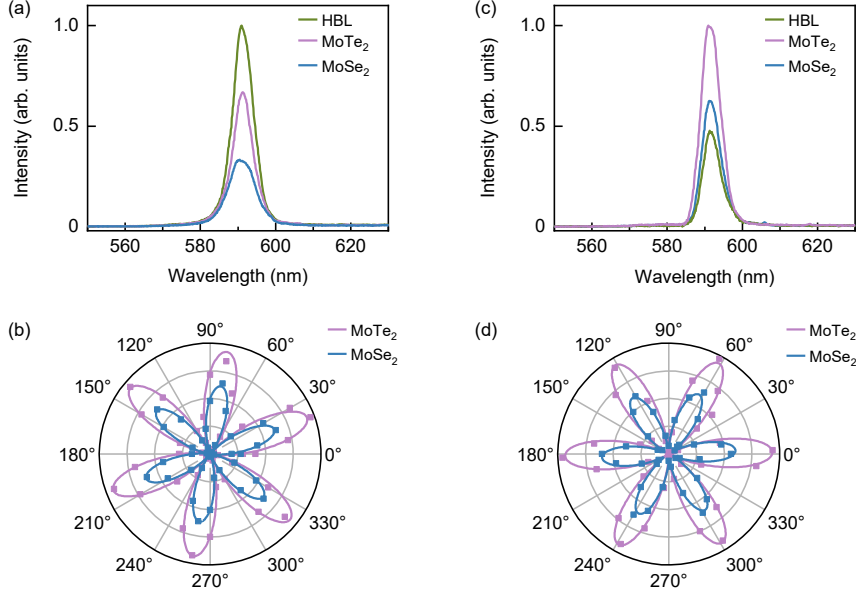


FIG. S2. Twist-angle measurements using second-harmonic generation. (a) SHG signal of an R-type heterobilayer measured on the monolayer MoSe₂, monolayer MoTe₂ and heterobilayer (HBL) parts with the same experimental configuration. (b) Polarization-resolved SHG intensity of monolayer MoSe₂ and MoTe₂ parts. The solid lines are the fits with sinusoidal functions. (c) and (d) Same measurements for an H-type heterobilayer sample.

the case of R-type ($\sim 0^\circ$) and H-type ($\sim 60^\circ$) bilayers cannot be differentiated by separately measuring the angle-resolved SHG of each constituent monolayer. To identify the type of R- or H-stacking, one has to additionally measure the SHG from the bilayer region. As exemplified in Fig. S2 (a) and (c), for the R-type (H-type) case the second harmonic fields of MoTe₂ and MoSe₂ layers constructively (destructively) interfere, making the SHG signal of the heterobilayer region stronger (weaker) than in the individual monolayer regions for the same experimental configuration. Note that the SHG signal of monolayer MoTe₂ is much stronger than that of monolayer MoSe₂, consistent with the higher second-order nonlinearity in compounds of telluride than that in compounds of selenide [10]. With the information on the stacking type, the angle-resolved SHG intensity patterns were fitted with $I_{\text{SHG}} \propto \cos^2[3(2\alpha - \phi)]$, where α is the rotation angle of the half-wave plate and ϕ is a fitting parameter defining the armchair orientation of the crystal. Thus, for R- and H-type heterobilayer, the twist angle θ between the two layers is determined by $\theta = |\phi_1 - \phi_2|$ and $\theta = 60^\circ - |\phi_1 - \phi_2|$, with ϕ_1 and ϕ_2 obtained from the fitting of the respective

monolayer regions. For the two representative heterobilayers in Fig. S2, the twist angles were determined as 2.0° and 58.1° , respectively. The twist angle uncertainty of this method was estimated to be $\sim 0.2^\circ$, from fitting uncertainties of the SHG patterns.

Supplementary Note 5: Sample homogeneity

For all samples studied in this work, we performed hyperspectral mapping of spatial homogeneity. Figure S3 and S4 show the results of a representative aligned R-type and H-type samples. Throughout the entire heterobilayer regions, the PL and absorption features vary only marginally with characteristics of X_1 and X_2 excitons. From the statistical analysis of the maps we find that the PL intensities of X_1 are relatively uniform with a typical fluctuation below 30%, and for both X_1 and X_2 peaks the dispersions of the energy positions

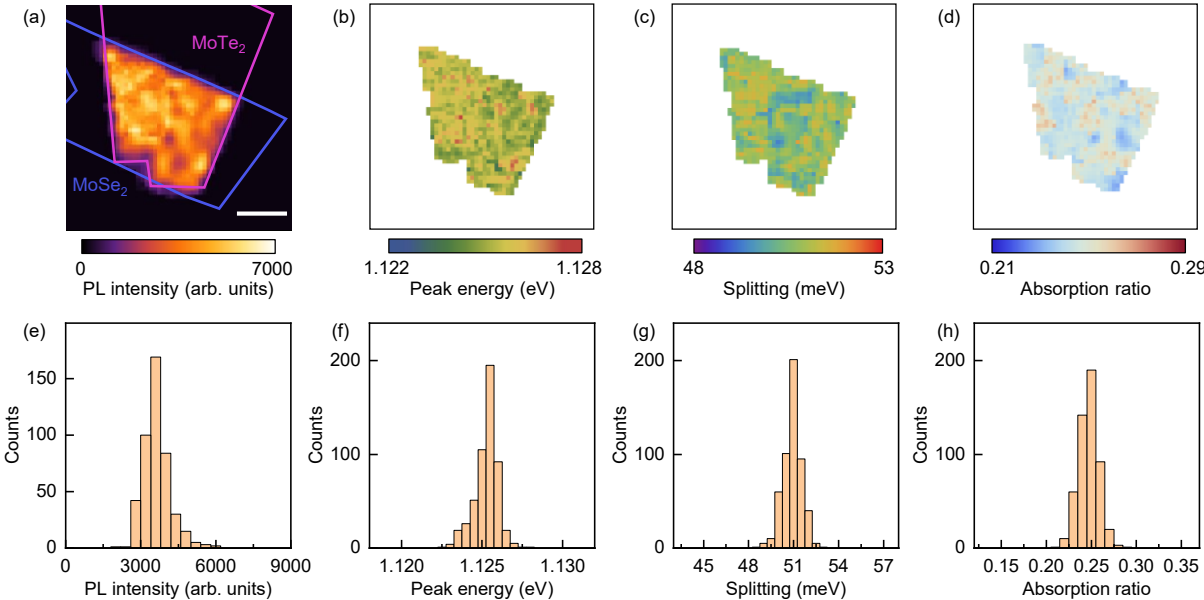


FIG. S3. Spatial maps of PL intensity (a) and peak energy (b) for X_1 exciton as well as the energy splitting (c) and absorption strength ratio (d) between X_1 and X_2 excitons, measured on the heterobilayer with 2° twist angle. The histograms in panels (e–h) show the statistics extracted from the maps in (a–d), respectively. The average PL intensity of peak X_1 in arbitrary units is 3843, with a standard deviation of 585. The average peak energy of X_1 and energy splitting between X_1 and X_2 are 1.125 eV and 51 meV, respectively, with the corresponding standard deviations of 2.1 and 1.8 meV. The average absorption strength ratio is 0.25 with a standard deviation of 0.02. The positions at the heterobilayer edges were excluded from the statistics. Scale bar in (a), 3 μm .

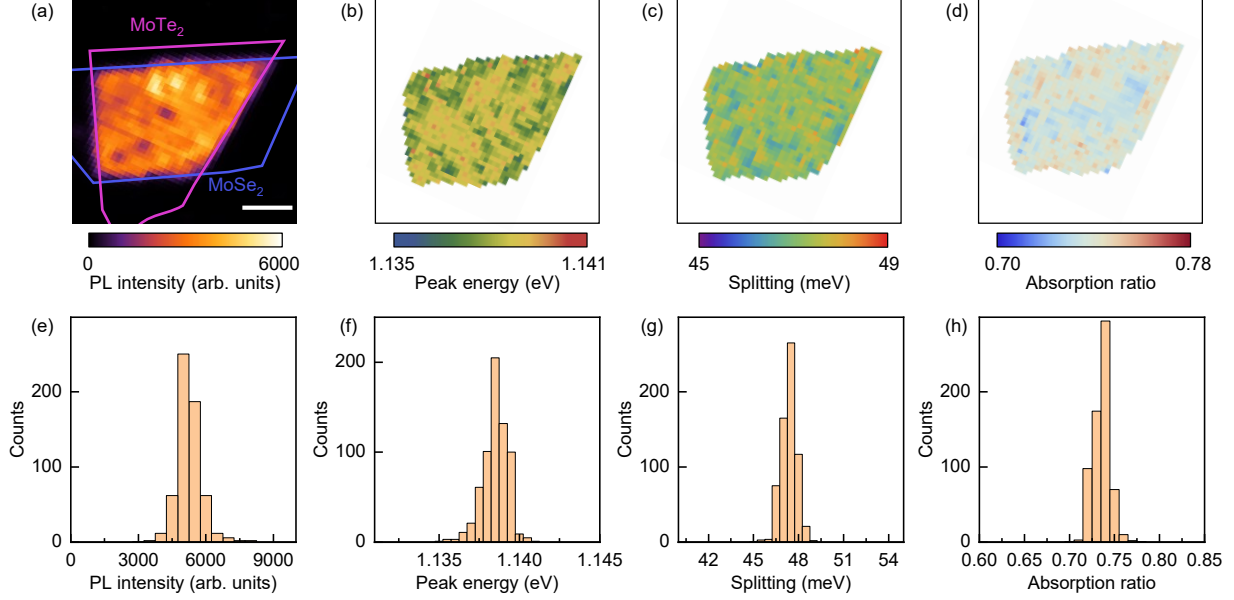


FIG. S4. Same as Fig. S3, measured on the heterobilayer with 58° twist angle. The average PL intensity (in arbitrary units), peak energy, energy splitting and absorption strength ratio are 5348, 1.138 eV, 47 meV and 0.74, respectively, with the corresponding standard deviations of 523, 2.7 meV, 1.9 meV and 0.02. Scale bar in (a), $4 \mu\text{m}$.

are smaller than 3 meV. Moreover, the variations of the energy splitting between the two peaks are also small (< 2 meV), and the same holds for their absorption strength ratio ($< 15\%$). The above results confirm the rather uniform optical characteristics of our devices, and rule out the formation of reconstructed domains in MoTe_2 - MoSe_2 heterobilayers signified by drastic spatial variations in the sample [5, 11]. The experimental data in Fig. 1(e) and (f) of the main text were obtained from statistical averaging of the corresponding spatial maps, and their standard deviations are represented as error bars.

Supplementary Note 6: Photoluminescence decay of hybrid excitons

To study the recombination dynamics of hybrid excitons, we performed time-resolved PL measurements on the lowest X_1 exciton transition for various heterobilayer twist angles. As the hybrid excitons have sizeable oscillator strength, their lifetimes become very short and comparable with the instrument response function (IRF) of our setup. To analyze the decay, we carried out iterative deconvolution fit by taking into account the IRF. In this way, we were able to determine measure lifetimes significantly smaller than the IRF [12]. As

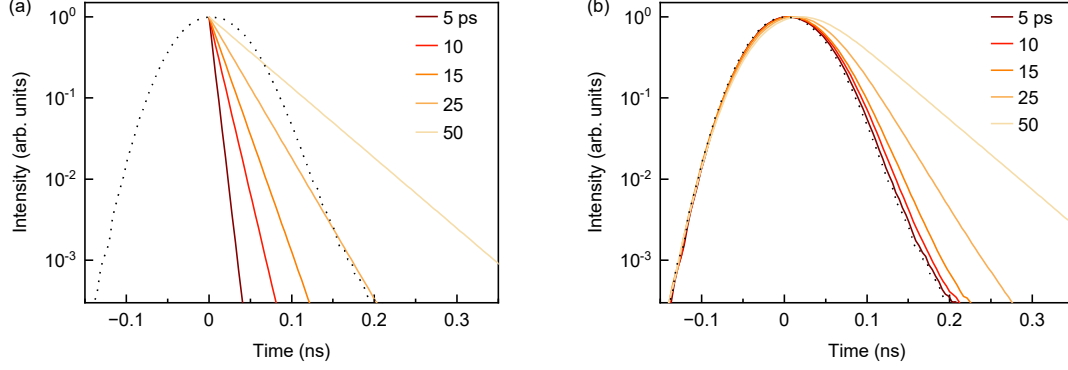


FIG. S5. Estimation of the temporal resolution for lifetime measurements. (a) and (b) Mono-exponential decay traces for different time constants (solid lines) before and after convolution with the instrument response function (dotted line), respectively. For time constant shorter than 10 ps, the decay traces become indistinguishable from the instrument response function.

illustrated in Fig. S5, the estimated temporal resolution limit of our setup using this fitting method is ~ 10 ps (compared to 100 ps for the FWHM of IRF). For shorter lifetimes, the decay traces overlap increasingly with the IRF, rendering the fit less reliable.

For almost aligned heterobilayers ($0^\circ \leq \theta \leq 7^\circ$ and $53^\circ \leq \theta \leq 60^\circ$), the lifetimes are long enough and the decay traces can be distinguished from the IRF. We used the reconvolution fitting method with bi-exponential function to fit these PL decays. As exemplified in Fig. S6(a) and (b), our fitting captures both the short and the long decay components with fitting residuals always below 5% and we found that the short component are always dom-

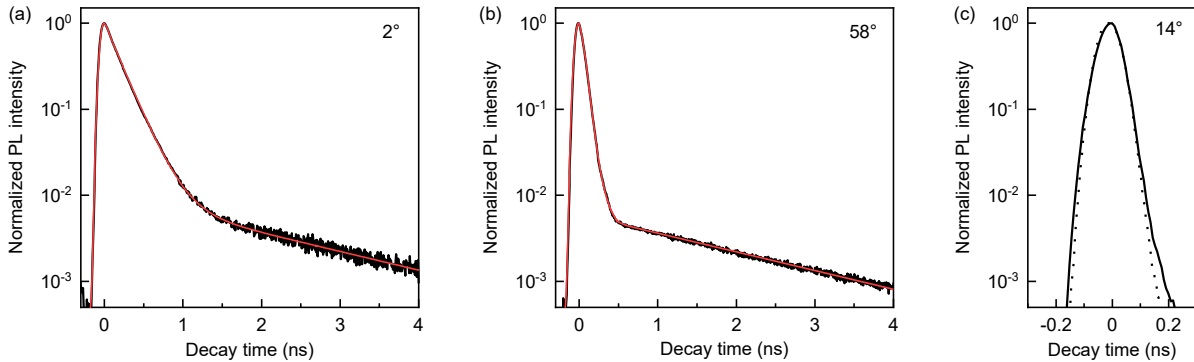


FIG. S6. Full-time-scale photoluminescence decays of hybrid X_1 exciton of heterobilayers with twist angles of 2° (a), 58° (b) and 14° (c). The red lines in (a) and (b) represent bi-exponential decay convoluted with the IRF as best fits. The dotted line in (c) corresponds to the IRF.

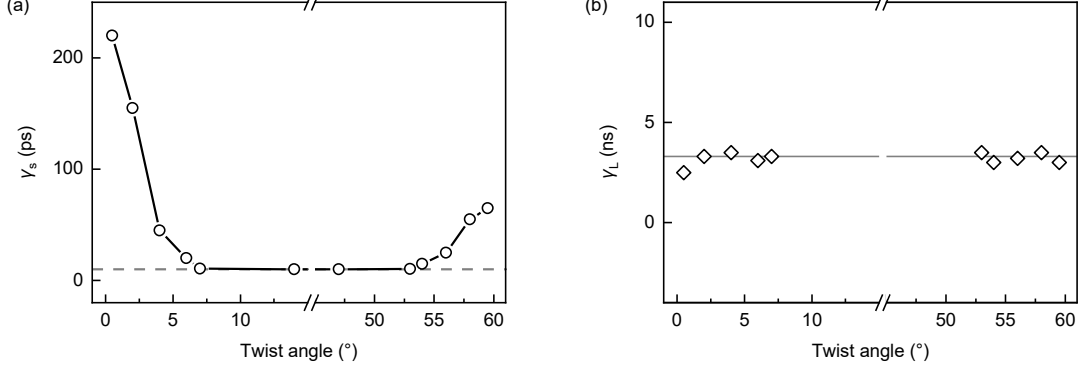


FIG. S7. (a) and (b) Short and long decay times of the X_1 exciton as a function of twist angle, respectively. Since the decay traces in misaligned heterobilayers ($7^\circ < \theta < 53^\circ$) are very short and overlap significantly with the IRF. We plotted the upper limit of their decay time in (a), which corresponds to the estimated temporal resolution limit of the setup (indicated by the dashed line).

inant (weight $> 95\%$) with a small contribution from the long component. For misaligned heterobilayers ($7^\circ < \theta < 53^\circ$), the decay traces is very short and overlaps with the IRF, as seen in Fig. S6(c). To a first approximation, we consider them as mono-exponential decays with the decay time equal to the resolution limit of 10 ps (on the same order of radiative lifetime for monolayer A-exciton [13]).

Figure S7 summarizes the obtained characteristic decay times γ_s and γ_L (corresponding to the short and long decay component, respectively) for different twist angles. By comparing with the plot in Fig. 1(f) of the main text, we found that the short decay time γ_s scales inversely with the oscillator strength of X_1 , and we thus associate this dominant decay component with the radiative recombination channel. In contrast, the long decay time γ_L remains relatively similar for all heterobilayer twist angles. We anticipated that this long component (several nanoseconds) with marginally contribution correspond to the non-radiative processes to the momentum-dark reservoir at the κ point [14].

Supplementary Note 7: Excitation power dependence of hybrid excitons

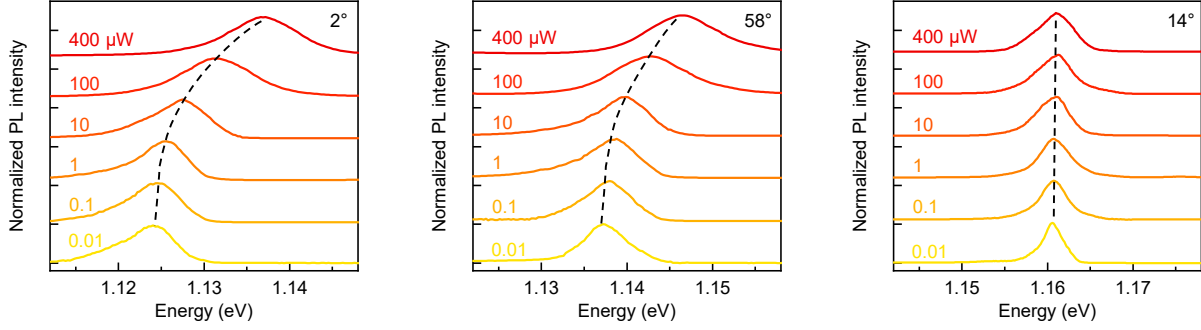


FIG. S8. Power-dependent PL spectra for the X_1 exciton in 2° , 58° and 14° twisted heterobilayers. The dashed lines highlight the energy evolution of peak maximum with power increasing. For the hybrid cases ($\theta = 2^\circ$ and 58°), the X_1 peak shows a continuous energy blue-shift with increased power by up to 15 and 10 meV, respectively. By comparison, for the non-hybrid case ($\theta = 14^\circ$), the peak remains almost non-shifted.

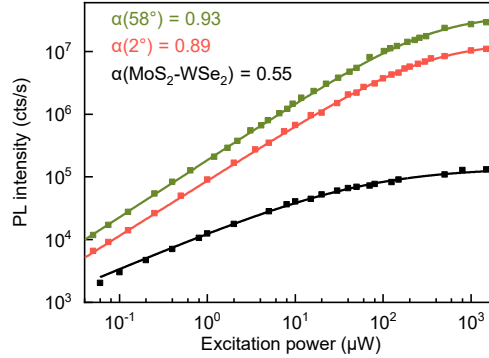


FIG. S9. Comparison of power-dependent PL intensity between the hybrid X_1 excitons in aligned MoTe_2 - MoSe_2 heterobilayers ($\theta = 2^\circ$ and 58° , red and green) and the pure interlayer exciton in an aligned MoS_2 - WSe_2 heterobilayer (black). The solid curves are fits to data (filled squares) using the saturation function $I = I_{\text{sat}}/(1 + P_{\text{sat}}/P^\alpha)$. We obtained almost linear scaling $\alpha = 0.89$ and 0.93 with the saturation powers P_{sat} of 160 and 210 μW and the saturation intensities I_{sat} of 1.3×10^7 and 3.9×10^7 counts s^{-1} for the hybrid excitons in 2° and 58° MoTe_2 - MoSe_2 , respectively. In contrast, for the interlayer exciton in MoS_2 - WSe_2 , the intensity starts to show a sub-linear response ($\alpha = 0.55$) from a very low power of 0.5 μW and becomes saturated around 10 μW with a saturation intensity of 2.8×10^5 counts s^{-1} , which is much lower than the hybridized excitons by a factor of ~ 100 . The measurements were conducted using the same setup.

Supplementary Note 8: Theoretical model of exciton hybridization

To model the experimental results, we applied the continuum model for near-resonant interlayer hybridization [15–17]. The MoTe₂-MoSe₂ heterobilayers facilitate the analysis of the lowest-energy excitons due to their substantial valence band offset ~ 0.5 eV [18]. On the other hand, their conduction bands are nearly aligned, therefore we focus on MoTe₂ intralayer excitons (X) and interlayer excitons (IX), which consist of a hole in MoTe₂ and an electron in MoSe₂. The twist angle θ and the lattice constant mismatch between two layers induce a valley mismatch represented by vectors $\Delta\mathbf{K} = \mathbf{K}_{\text{Se}} - \mathbf{K}_{\text{Te}}$ and $\Delta\mathbf{K} = \mathbf{K}'_{\text{Se}} - \mathbf{K}_{\text{Te}}$ for R- and H-type heterobilayers, respectively. The emergent periodicity of the moiré superlattice leads to the formation of a mini Brillouin zone (mBZ) with reciprocal basis vectors

$$\mathbf{b}_{1,2} = \frac{\sqrt{3}}{2} \begin{bmatrix} \sqrt{3} & \pm 1 \\ \mp 1 & \sqrt{3} \end{bmatrix} \Delta\mathbf{K}. \quad (1)$$

We define the mBZ as shown in Fig. S10 with the center γ at the K -valley of MoTe₂ (\mathbf{K}_{Te}), and the point κ at the K - or K' -valley of MoSe₂. With this definition of the mBZ, the momentum-direct excitons are located at the γ point.

Following the model from Ref. 15, we introduce the Hamiltonian

$$H = \begin{pmatrix} H_X & T \\ T^* & H_{\text{IX}} \end{pmatrix}, \quad (2)$$

where we assume parabolic dispersions of intralayer and interlayer excitons, with the corresponding diagonal blocks are written as follows:

$$\langle X, \mathbf{k} + \mathbf{g}' | H_X | X, \mathbf{k} + \mathbf{g} \rangle = \delta_{\mathbf{g}, \mathbf{g}'} \left(E_X + \frac{\hbar^2 |\mathbf{k} + \mathbf{g}|^2}{2M_X} \right) + \sum_{j=1}^6 V_j \delta_{\mathbf{g}, \mathbf{g}' + \mathbf{G}_j}, \quad (3)$$

$$\langle \text{IX}, \mathbf{k}' + \mathbf{g}' | H_{\text{IX}} | \text{IX}, \mathbf{k}' + \mathbf{g} \rangle = \delta_{\mathbf{g}, \mathbf{g}'} \left(E_{\text{IX}} + \frac{\hbar^2 |\mathbf{k} + \mathbf{g}'|^2}{2M_{\text{IX}}} \right), \quad (4)$$

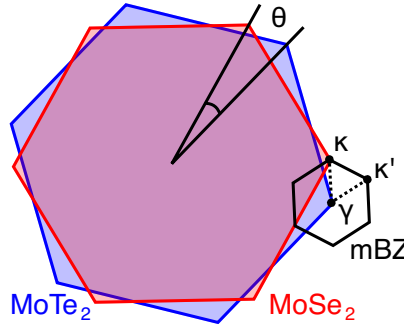


FIG. S10. Formation of a mini Brillouin zone in MoTe₂-MoSe₂ heterobilayer.

where the reciprocal vectors are $\mathbf{g} = n\mathbf{b}_1 + m\mathbf{b}_2$, n and m are integers, \mathbf{k} and \mathbf{k}' are the center-of-mass wave vectors of X and IX excitons measured from γ and κ , respectively; $E_{X(\text{IX})}$ and $M_{X(\text{IX})}$ are the respective energies and effective masses; $V_1 = V_3 = V_5 \equiv V$ and $V_2 = V_4 = V_6 \equiv V^*$ characterize the lowest-order harmonic expansion of the electron moiré potential in MoTe₂ with the first-shell reciprocal lattice vectors \mathbf{G}_j ($j = 1, 2, \dots, 6$). We assume that the moiré potentials for holes in MoTe₂ and for electrons in MoSe₂ are relatively small and we neglect their contributions in model [15]. In Table S1 we summarize the relevant parameters for the singlet and triplet excitons, which are further considered independently.

The tunneling of conduction band electrons is described by interlayer hopping elements

$$\langle \text{IX}, \mathbf{k}' + \mathbf{g}' | T | X, \mathbf{k} + \mathbf{g} \rangle = t(\delta_{\mathbf{k}+\mathbf{g}, \mathbf{k}'+\mathbf{g}'+\Delta\mathbf{K}} + \delta_{\mathbf{k}+\mathbf{g}, \mathbf{k}'+\mathbf{g}'+C_3^1\Delta\mathbf{K}} + \delta_{\mathbf{k}+\mathbf{g}, \mathbf{k}'+\mathbf{g}'+C_3^2\Delta\mathbf{K}}), \quad (5)$$

with the hopping parameter t , and rotation matrix C_ν^μ with angle $2\pi\mu/\nu$.

The diagonalization of the Hamiltonian in Eq. (2) provides eigenenergies and eigenvectors of hybrid moiré states. We assume that their oscillator strengths are proportional to the squared norm of their projections onto the fundamental A-exciton state. In our analysis, E_0 , Δ , V and t are treated as free parameters, and other band parameters are obtained from our *ab initio* calculations (see Supplementary Note 10). By fitting the model to twist-dependent data shown in Figs. 1(c-f), we reproduce the energies and oscillator strengths of the two moiré excitons with very good agreement, with $E_0 = 1162$ meV, $\Delta = -54$ meV, and $t = 12$ meV.

type	spin state	E_X	E_{IX}	M_X	M_{IX}
R	singlet	E_0	$E_0 + \Delta$	$m_c + m_v$	$m'_c + m_v$
R	triplet	$E_0 + \Delta_{\text{SO}}$	$E_0 + \Delta + \Delta'_{\text{SO}}$	$m_{c+1} + m_v$	$m'_{c+1} + m_v$
H	singlet	E_0	$E_0 + \Delta + \Delta'_{\text{SO}}$	$m_c + m_v$	$m'_{c+1} + m_v$
H	triplet	$E_0 + \Delta_{\text{SO}}$	$E_0 + \Delta$	$m_{c+1} + m_v$	$m'_c + m_v$

TABLE S1. Energies and effective masses of intralayer and interlayer excitons. E_0 is the A-exciton energy in MoTe₂ monolayer, and Δ is the energy offset between interlayer and intralayer excitons. The effective mass parameters m_c , m_{c+1} , m_v and the spin-orbit splitting Δ_{SO} correspond to the MoTe₂ layer, whereas the effective mass parameters m'_c , m'_{c+1} and the spin-orbit splitting Δ'_{SO} are related to the MoSe₂ layer. In our model, E_0 and Δ are fitting parameters, and all other parameters are obtained from our *ab initio* calculations (see Table S2).

For the fitting procedure, we employed the method of least squares and simultaneously minimized the respective squares of the exciton energies E_i and oscillator strengths f_i . With dimensionless energies, obtained from normalization by the spectral window of 40 meV, we minimized the function $\mathcal{F} = \sum_{\theta_j} [[(E - E_i)/40 \text{ meV}]^2 + (f - f_i)^2]$, where we sum over all experimental values of twist angles θ_j . Intralayer potentials for R-type and H-type stackings have the same amplitude $|V| = 1 \text{ meV}$, but different phases, $\arg(V) = 3\pi/4$ and $7\pi/12$, respectively. In our fitting procedure, we find that the parameter $|V|$ in the range between 0 and 3 meV leads to approximately the same residuals. To obtain the best-fit value for this parameter, we take into account the constrains of phases $\arg(V)$, depending on the trion binding energy results from the charge-doping experiments on 2° and 58° samples.

In Fig. 4(c) and (d) of the main text, we plot the potential linecuts along the main diagonal of the moiré unit cell using the following real-space representation:

$$\mathcal{V}(\mathbf{r}) = \sum_{j=1}^6 V_j e^{i\mathbf{G}_j \mathbf{r}}. \quad (6)$$

In the same way we compute the real-space distributions of the intralayer contributions to the hybrid moiré excitons [15], shown in Fig. 4(e) and (f) of the main text for X_1 ($m = 1$) and X_2 ($m = 2$) states in $\theta = 2^\circ$ and 58° heterobilayers:

$$\psi_m(\mathbf{r}) = \sum_{\mathbf{G}_l \in \mathbf{G}} c_{lm} e^{i\mathbf{G}_l \mathbf{r}}, \quad (7)$$

where we use the obtained eigenvectors c_{lm} and sum over corresponding wave vectors of intralayer states in the calculation of \mathbf{G} .

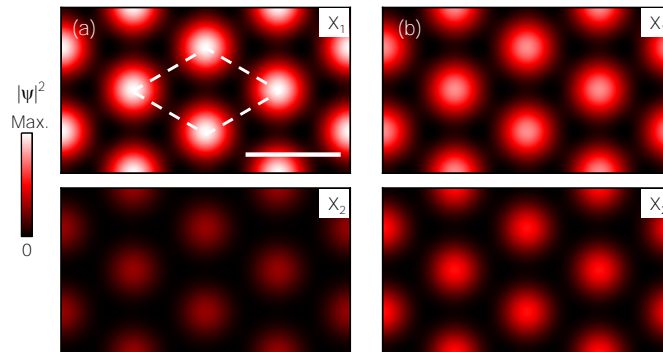


FIG. S11. Color-coded maps of real-space probability functions $|\psi|^2$ of interlayer excitons contributing to X_1 (upper panel) and X_2 (lower panel) excitons in heterostacks with twist angles of (a) 2° and (b) 58° . The dashed rhombus indicates the moiré unit cell, the scale bars are 5 nm.

Accordingly, in Fig. S11 we show the real-space distributions of the interlayer contributions to hybrid moiré excitons obtained from the following equation:

$$\psi_m^{\text{IX}}(\mathbf{r}) = \sum_{\mathbf{G}_l \in \mathbf{G}^{\text{IX}}} c_{lm}^{\text{IX}} e^{i\mathbf{G}_l \mathbf{r}}, \quad (8)$$

where the eigenvectors c_{lm}^{IX} and wave vectors \mathbf{G}^{IX} correspond to the interlayer states.

Supplementary Note 9: Dependence of hybrid excitons on twist angle

Figure S12 displays the calculated hybrid exciton band structures together with the decoupled MoTe₂ A-exciton (X_A) and spin-singlet interlayer exciton (IX) bands for various twist angles. Owing to the small conduction band offset between MoTe₂ and MoSe₂, the two decoupled bands cross inside the mini Brillouin zone. In our model, introducing interlayer tunneling results in avoided crossing of the bands due to hybridization of their X_A and IX characters. The resonance of hybridization with equal composition of the two characters occurs at the position where the two decoupled bands cross. Away from this position, the degree of hybridization gradually reduces and the bands recover their original character. As shown in Fig. S12, the position of the band crossing evolves with the twist angle due to the modification of moiré geometry, and at the same time, the energy of the IX band at the γ point shifts. Since the optically active X_A and IX hybridized states (X_1 and X_2) are located at the γ point, their energies and oscillator strengths display twist-angle dependence.

The above evolution of exciton hybridization can be divided into several limits, which we elaborate for the R-type stacking. For the case of R-type: (i) When twist angle $\theta = 0^\circ$, the decoupled IX and X_A bands cross on the right side of the γ point and the IX band is below X_A at the γ point. As a result, the lower energy hybridized exciton state X_1 has more IX character and the higher energy state X_2 has more X_A character, implying a smaller oscillator strength of X_1 as compared to X_2 . (ii) When θ increases, the position of the band crossing in momentum space moves towards the γ point and the hybridization becomes stronger, transferring the oscillator strength from X_2 to X_1 state and pushing the X_2 state to higher energy. Note that because the decoupled IX band moves up at the γ point, the X_1 state is also blue-shifted. (iii) When θ reaches 4.6° , the band crossing takes place exactly at the γ point, giving rise to maximal hybridization. The X_1 and X_2 states have equal IX and X_A characters and thus the same oscillator strength at this twist angle. (iv) When θ continues to increase, the band crossing position moves away to the left side of the γ point

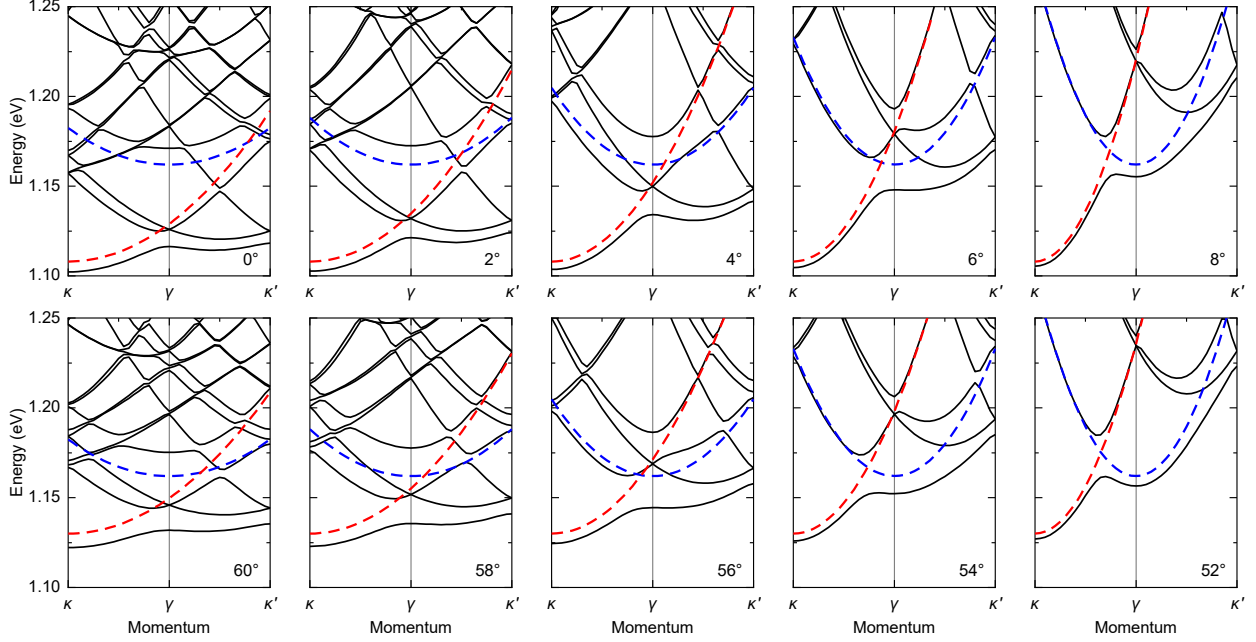


FIG. S12. Moiré band structures of hybridized excitons in MoTe₂-MoSe₂ heterobilayers calculated for different interlayer twist angles. The panels depict only spin-bright (singlet) hybridized exciton bands within the first moiré Brillouin zone. Red and blue dashed lines in all panels represent the uncoupled MoTe₂ A-exciton and the interlayer exciton IX states.

and the decoupled IX and X_A bands reverse the energy ordering at this point. Consequently, X₁ becomes more in X_A character, while X₂ has more IX character. The oscillator strength of X₁ (X₂) thus increases (decreases). Meanwhile, the energy of X₂ state increases as the decoupled IX band moves up at the γ point. The energy of the X₁ state also increases because of the reduced degree of hybridization and less avoided crossing at the γ point. (v) When $\theta \gtrsim 8^\circ$, the band crossing position is too far away from the γ point and the degree of hybridization becomes vanishingly small. As a result, X_A and IX bands are fully uncoupled and only one exciton state that corresponds to the A-exciton of MoTe₂ is optically active (the pure IX state has negligible oscillator strength). In this twist angle range, the energy and oscillator strength of the single exciton state show almost no variations. For H-type, the trend is similar to R-type, but the hybridized excitons have higher energies as the spin-singlet IX and X_A are energetically closer due to the flipped spin-ordering of IX bands. In addition, the starting degree of hybridization at 60° is higher and the maximal hybridization takes place for a smaller deviation from ideal anti-parallel alignment at an angle of 57.2°.

Supplementary Note 10: Density functional theory

The theoretical simulations of the band dispersion parameters and the g -factors were performed using density functional theory (DFT) on the level of the Perdew-Becke-Ernzerhof (PBE) approximation as implemented in the Quantum Espresso package [19]. The core electrons were replaced by fully-relativistic normconserving pseudopotentials from the PseudoDojo library [20], where the s and p semi-core electrons of Mo are included in the set of valence electrons. As a preliminary step, we optimized the atomic positions and the in-plane lattice constants of isolated MoSe₂ and MoTe₂ monolayers until the interatomic forces and the stress were below thresholds of 0.01 eV/Å and 0.01 GPa, respectively, while keeping a vacuum layer of at least 15 Å in the out-of-plane direction in order to minimize interactions between periodic images. We included semi-empirical van der Waals corrections from the PBE+D3 scheme [21], which yields excellent predictions of the in- and out-of-plane lattice constants of layered systems. Integrations in reciprocal space were performed on a Monkhorst-Pack grid of $12 \times 12 \times 1$ points in the Brillouin zone. In this step, we did not explicitly include spin-orbit interactions (SOI). Based on the obtained optimized structure, we then simulated the electronic band energies, the corresponding Kohn-Sham orbitals and the interband optical matrix elements, and the vacuum level energies of the monolayers on the PBE level, with full inclusion of spin-orbit interactions. From the obtained bandstructures, we then derived the effective masses and orbital angular momenta of the relevant valence and conduction bands [22]. For the orbital angular momenta, the sum over states was performed over 2000 valence and conduction bands. Using Eq. 2 in the main text, we obtained a g -factor of -4.6 and -4.3 for the A-exciton in monolayer MoTe₂ and MoSe₂, in excellent agreement with the experimental results (see Fig. S1).

	m_c/m_0	m_{c+1}/m_0	m_v/m_0	Δ_{SO}	L_c	L_{c+1}	L_v
MoTe ₂	0.58	0.67	-0.68	69	1.586	1.204	3.872
MoSe ₂	0.55	0.63	-0.64	23	1.798	1.526	3.977

TABLE S2. Material parameters at the K points from DFT calculations. m_c (m_{c+1}) is the effective electron mass of the first (second) conduction band with free electron mass m_0 ; m_v is the effective mass of the highest valence band; Δ_{SO} is the spin-orbit splitting in the conduction band, in units of meV. L_c and L_{c+1} are the orbital angular momenta of the first and second conduction bands, and L_v is the orbital angular momentum of the highest valence band.

Supplementary References

- [1] F. Pizzocchero, L. Gammelgaard, B. S. Jessen, J. M. Caridad, L. Wang, J. Hone, P. Bøggild, and T. J. Booth, The hot pick-up technique for batch assembly of van der Waals heterostructures, *Nat. Commun.* **7**, 11894 (2016).
- [2] S. Liu, Y. Liu, L. Holtzman, B. Li, M. Holbrook, J. Pack, T. Taniguchi, K. Watanabe, C. R. Dean, A. N. Pasupathy, K. Barmak, D. A. Rhodes, and J. Hone, Two-step flux synthesis of ultrapure transition-metal dichalcogenides, *ACS Nano* **17**, 16587 (2023).
- [3] E. M. Alexeev, A. Catanzaro, O. V. Skrypkina, P. K. Nayak, S. Ahn, S. Pak, J. Lee, J. I. Sohn, K. S. Novoselov, H. S. Shin, and A. I. Tartakovskii, Imaging of interlayer coupling in van der waals heterostructures using a bright-field optical microscope, *Nano Lett.* **17**, 5342 (2017).
- [4] P. Back, M. Sidler, O. Cotlet, A. Srivastava, N. Takemura, M. Kroner, and A. Imamoglu, Giant paramagnetism-induced valley polarization of electrons in charge-tunable monolayer MoSe₂, *Phys. Rev. Lett.* **118**, 237404 (2017).
- [5] S. Zhao, Z. Li, X. Huang, A. Rupp, J. Göser, I. A. Vovk, S. Y. Kruchinin, K. Watanabe, T. Taniguchi, I. Bilgin, A. S. Baimuratov, and A. Högele, Excitons in mesoscopically reconstructed moiré heterostructures, *Nat. Nanotechnol.* **18**, 572 (2023).
- [6] F. Cadiz, E. Courtade, C. Robert, G. Wang, Y. Shen, H. Cai, T. Taniguchi, K. Watanabe, H. Carrere, D. Lagarde, M. Manca, T. Amand, P. Renucci, S. Tongay, X. Marie, and B. Urbaszek, Excitonic linewidth approaching the homogeneous limit in MoS₂-based van der Waals heterostructures, *Phys. Rev. X* **7**, 021026 (2017).
- [7] D. Edelberg, D. Rhodes, A. Kerelsky, B. Kim, J. Wang, A. Zangiabadi, C. Kim, A. Abhinandan, J. Ardelean, M. Scully, D. Scullion, L. Embon, R. Zu, E. J. G. Santos, L. Balicas, C. Marianetti, K. Barmak, X. Zhu, J. Hone, and A. N. Pasupathy, Approaching the intrinsic limit in transition metal diselenides via point defect control, *Nano Lett.* **19**, 4371 (2019).
- [8] A. Arora, R. Schmidt, R. Schneider, M. R. Molas, I. Breslavetz, M. Potemski, and R. Bratschitsch, Valley Zeeman splitting and valley polarization of neutral and charged excitons in monolayer MoTe₂ at high magnetic fields, *Nano Lett.* **16**, 3624 (2016).
- [9] M. Goryca, J. Li, A. V. Stier, T. Taniguchi, K. Watanabe, E. Courtade, S. Shree, C. Robert, B. Urbaszek, X. Marie, and S. A. Crooker, Revealing exciton masses and dielectric properties of monolayer semiconductors with high magnetic fields, *Nat. Commun.* **10**, 4172 (2019).

- [10] Y. R. Shen, *Principles of nonlinear optics* (Wiley, 1984).
- [11] S. Shabani, D. Halbertal, W. Wu, M. Chen, S. Liu, J. Hone, W. Yao, D. N. Basov, X. Zhu, and A. N. Pasupathy, Deep moiré potentials in twisted transition metal dichalcogenide bilayers, *Nat. Phys.* **17**, 720 (2021).
- [12] D. O'Connor and D. Phillips, *Time-correlated Single Photon Counting* (Elsevier Science, 1984).
- [13] H. H. Fang, B. Han, C. Robert, M. A. Semina, D. Lagarde, E. Courtade, T. Taniguchi, K. Watanabe, T. Amand, B. Urbaszek, M. M. Glazov, and X. Marie, Control of the exciton radiative lifetime in van der Waals heterostructures, *Phys. Rev. Lett.* **123**, 067401 (2019).
- [14] B. Miller, A. Steinhoff, B. Pano, J. Klein, F. Jahnke, A. Holleitner, and U. Wurstbauer, Long-lived direct and indirect interlayer excitons in van der Waals heterostructures, *Nano Lett.* **17**, 5229 (2017).
- [15] B. Polovnikov, J. Scherzer, S. Misra, X. Huang, C. Mohl, Z. Li, J. Göser, J. Förste, I. Bilgin, K. Watanabe, T. Taniguchi, A. Högele, and A. S. Baimuratov, Field-induced hybridization of moiré excitons in MoSe₂/WS₂ heterobilayers, *Phys. Rev. Lett.* **132**, 076902 (2024).
- [16] D. A. Ruiz-Tijerina and V. I. Fal'ko, Interlayer hybridization and moiré superlattice minibands for electrons and excitons in heterobilayers of transition-metal dichalcogenides, *Phys. Rev. B* **99**, 125424 (2019).
- [17] F. Wu, T. Lovorn, and A. H. MacDonald, Topological exciton bands in moiré heterojunctions, *Phys. Rev. Lett.* **118**, 147401 (2017).
- [18] C. Zhang, C. Gong, Y. Nie, K.-A. Min, C. Liang, Y. J. Oh, H. Zhang, W. Wang, S. Hong, L. Colombo, R. M. Wallace, and K. Cho, Systematic study of electronic structure and band alignment of monolayer transition metal dichalcogenides in van der Waals heterostructures, *2D Mater.* **4**, 015026 (2016).
- [19] P. Giannozzi, S. Baroni, N. Bonini, M. Calandra, R. Car, C. Cavazzoni, D. Ceresoli, G. L. Chiarotti, M. Cococcioni, I. Dabo, A. D. Corso, S. de Gironcoli, S. Fabris, G. Fratesi, R. Gebauer, U. Gerstmann, C. Gougoussis, A. Kokalj, M. Lazzeri, L. Martin-Samos, N. Marzari, F. Mauri, R. Mazzarello, S. Paolini, A. Pasquarello, L. Paulatto, C. Sbraccia, S. Scandolo, G. Sclauzero, A. P. Seitsonen, A. Smogunov, P. Umari, and R. M. Wentzcovitch, Quantum espresso: a modular and open-source software project for quantum simulations of materials, *J. Phys.: Condens. Matter* **21**, 395502 (2009).

- [20] M. van Setten, M. Giantomassi, E. Bousquet, M. Verstraete, D. Hamann, X. Gonze, and G.-M. Rignanese, The pseudodojo: Training and grading a 85 element optimized norm-conserving pseudopotential table, *Comput. Phys. Commun.* **226**, 39 (2018).
- [21] S. Grimme, S. Ehrlich, and L. Goerigk, Effect of the damping function in dispersion corrected density functional theory, *J. Comput. Chem.* **32**, 1456 (2011).
- [22] T. Deilmann, P. Krüger, and M. Rohlfing, Ab initio studies of exciton g factors: Monolayer transition metal dichalcogenides in magnetic fields, *Phys. Rev. Lett.* **124**, 226402 (2020).